ADVANCED OPTICAL MATERIALS
www.advopticalmat.de

Control Over the Microstructure of Vapor-Deposited $CsPbBr_3$ Enhances Amplified Spontaneous Emission

*Qimu Yuan, Weilun Li, Ford M. Wagner, Vincent J.-Y. Lim, Laura M. Herz, Joanne Etheridge, and Michael B. Johnston**

Inorganic cesium-based metal halide perovskite (MHP) semiconductors have great potential as active layers in optoelectronic devices, such as perovskite light-emitting diodes (PeLEDs) and perovskite lasers. However, precise control of crystal type, quality, and thickness is required to create high-performance and reproducible devices. Vapor-phase vacuum deposition enables fabrication of MHP thin films and devices with excellent uniformity and control over layer thickness, although a full understanding of crystal growth mechanisms and products has proved elusive. Here, conditions of vapor co-deposition of CsBr and PbBr are related with the optical performance and atomic microstructure of resulting $CsPbBr_3$ thin films. It is found that the structure is predominantly photoactive γ-$CsPbBr_3$ over a wide range of conditions, but the presence of impurity phases and Ruddlesden–Popper (RP) planar defects both degrade optical performance as quantified through measured amplified spontaneous emission (ASE) thresholds. Furthermore, the atomic structure of the dominant impurity phases is resolved: $CsPb_2Br_5$ and Cs_4PbBr_6. It is revealed that a small nominal excess of CsBr-precursor flux during co-evaporation can significantly enhance the nucleation of thin films, resulting in well-defined grains greater than 500 nm in size and the relative suppression of RP planar defects. Such films exhibit intensified photoluminescence (PL) emission and a reduced ASE threshold of 30.9 μJ cm^{-2}.

1. Introduction

In the last decade, MHPs have emerged as excellent candidates of both efficient photovoltaic absorbers and luminescent light-emission mediums.[1–4] The outstanding properties of MHPs, such as high photoluminescence quantum yield (PLQY), tuneable emission wavelengths with suitable linewidths, and long charge-carrier diffusion length, have poised PeLEDs as a favorable display technology.[5–7] In addition, the impressive optical gain coefficient, high refractive index, and strong inter-band absorption of MHPs, have facilitated the rapid development of optically driven perovskite lasers with different cavity designs.[8–11]

In particular, all-inorganic MHPs of $CsPbX_3$ (X = Br, Cl, or I) have garnered significant attention as competent gain mediums in designs of distributed feedback cavity,[12,13] distributed Bragg reflector cavity,[14,15] and Fabry-Perot cavity[16,17] lasers. Compared with their organic-inorganic counterparts, MHPs of $CsPbX_3$, especially $CsPbBr_3$, exhibit enhanced thermal stability and structural durability as volatile and hygroscopic organic cations of formamidinium and methylammonium are avoided.[8,18,19] Nevertheless, the majority of recently reported inorganic MHP gain mediums are deposited through lab-based solution-processing methods, which may be less applicable for the scalability and reproducibility required from industrial-scale fabrication.[4,20]

Alternatively, vapor deposition is an established vacuum technique enabling the solvent-free processing of MHP thin films through either multi-source co-evaporation or sequential

---

Q. Yuan, F. M. Wagner, V. J.-Y. Lim, L. M. Herz, M. B. Johnston
Department of Physics
University of Oxford
Clarendon Laboratory
Parks Road, Oxford OX1 3PU, UK
E-mail: michael.johnston@physics.ox.ac.uk

The ORCID identification number(s) for the author(s) of this article can be found under https://doi.org/10.1002/adom.202502160

DOI: 10.1002/adom.202502160

W. Li, J. Etheridge
School of Physics and Astronomy
Monash University
Melbourne, VIC 3800, Australia

J. Etheridge
Monash Centre for Electron Microscopy
Monash University
Melbourne, VIC 3800, Australia

J. Etheridge
Department of Materials Science and Engineering
Monash University
Melbourne, VIC 3800, Australia

sublimation of individual precursors.[21–24] Vapor deposition is well suited to the fabrication of perovskite gain mediums and their incorporation into often complex and delicate optical cavities for a broad range of reasons including i) excellent uniformity and morphology over large areas, ii) the capability to grow multiple layers of different thin films without affecting any underlying layers, and iii) the flexibility to tune the deposited layer thickness precisely and reproducibly from tens of nanometres to over a micron.[20,25–28] Moreover, vapor-based processing is widely employed in commercial semiconductor fabrication, for example organic light-emitting diodes and displays, which offers promising prospects for the future up-scaling of MHP-based optoelectronics and lasers.[10,21]

Although less commonly reported, vapor-deposited $CsPbBr_3$ thin films have been shown to exhibit amplified spontaneous emission (ASE) characteristics and were successfully incorporated into different laser cavities with a low lasing threshold.[10,14,29] For example, Huang et al. recently presented a vertical surface-emitting laser cavity with $CsPbBr_3$ sandwiched between layers of SiO_2. They achieved a lasing threshold of 13 $\mu J\ cm^{-2}$ by passivating defects in the gain medium by introducing triphenylphosphine oxide (TPPO) during the MHP co-evaporation.[10] Indeed, passivation of the vapour-deposited $CsPbBr_3$ layer with organics, such as TPPO, polyethylene oxide, 2-phenylethanamine bromide are typically employed in the parallel PeLED research in regulating crystallization dynamics, controlling perovskite morphology and dimensionality, and spatially confining charge-carriers to enhance emission efficiency.[30–32] However, the use of organic additives will likely hinder the thermal stability of MHPs, especially under high-temperature optical-pumping operations.[5] In addition, for organics, owing to their low evaporation temperature (≈<100 °C) and undesirable sublimation dynamics of condensing partially outside the evaporation cone, even a small flux of organics vapor will often result in the possibility of chamber contamination. Therefore, alternative approaches in optimizing vapor-deposited $CsPbBr_3$ as a laser gain medium need to be considered.

A viable and facile method to improve the optical performance of $CsPbBr_3$ films formed by co-evaporation of CsBr and $PbBr_2$ is the direct tuning of the molar precursor flux ratio of CsBr to $PbBr_2$ (abbreviated as Cs:Pb flux ratio here on) during film growth.[29,33] Under either Pb-rich or Cs-rich preparation conditions, impurity phases of $CsPb_2Br_5$ or Cs_4PbBr_6 will form respectively, in addition to $CsPbBr_3$.[5] It has been reported that these impurity phases can enhance the emission efficiency of $CsPbBr_3$ thin films in PeLEDs, either from the confinement of charge-carriers owing to the wider bandgap of impurities or from the surface passivation of non-radiative recombination centres by Cs_4PbBr_6.[5,34] Moreover, Bolink et al. recently reported that the formation of $CsPb_2Br_5$ impurity will encase the single-source thermal-evaporated $CsPbBr_3$ perovskites, leading to undesirable effects of quantum confinement.[35] As the ASE performance of a laser gain medium is highly correlated with the stoichiometric composition, morphology, grain size and boundary, and crystal defects,[10,14,33,36] it is important to scrutinize vapor-deposited $CsPbBr_3$ and assess the role of its impurity phases in relation to these factors.

Transmission electron microscopy (TEM) is a powerful technique for revealing the atomic structure of materials.[37] However, its application to halide perovskites has been limited by electron beam-induced damage.[38] In particular, structural studies of $CsPbBr_3$ and its impurity phases, $CsPb_2Br_5$ and Cs_4PbBr_6—which could offer valuable insights into phase formation and control during crystal growth—remain scarce. We have recently reported the presence of RP planar defects, which acts as a major source of non-radiative recombination centers, in vapor-deposited γ-$CsPbI_3$ thin films under Cs-excess co-evaporation conditions, even with a molar CsI:PbI_2 precursor flux ratio as little as 1.03.[39] As γ-$CsPbBr_3$ has the homologous unit cell structure as γ-$CsPbI_3$, it is critical to examine the role of RP defects in influencing the ASE performance of $CsPbBr_3$ films with Cs-excess.

In this work, we systemically tuned the nominal Cs:Pb precursor flux ratio during co-evaporation of $CsPbBr_3$ perovskite films from Cs-deficient to Cs-rich, and we examined the impact on crystal growth and spontaneous emission (SE). Utilizing scanning transmission electron microscopy (STEM), we reveal stunning differences in thin-film crystallization by resolving atomic microstructures. We highlight that $CsPbBr_3$ films grown with a Cs-deficiency led to the formation of $CsPb_2Br_5$ impurity phase and undesirable morphology including "snowflake"-like features, indicating insufficient nucleation. At the other extreme, $CsPbBr_3$ film growth under excessively Cs-rich conditions results not just in the Cs_4PbBr_6 impurity phase, but also a high density of RP planar faults and inconsistent microstructures. As a result, co-evaporated films with both Cs-deficient and significant Cs-excess precursor fluxes exhibit poor optoelectronic properties and high ASE thresholds. In contrast, we elucidate that a Cs:Pb precursor flux ratio of 1.5:1 yielded intensified PL emission and optimized ASE performance, which we attribute to the microstructural and atomistic prerequisites of complete crystallization, homogenous surface morphology, and relative suppression of impurities and planar defects. This study demonstrates a facile method in optimizing vapor co-deposited $CsPbBr_3$ thin films for laser applications, and more importantly, unveils novel interconnections between ASE thresholds and atomic structures.

2. Results and Discussion

2.1. Tuning of Cs:Pb Precursor Flux Ratios

We prepared two sets of co-evaporated $CsPbBr_3$ thin films (35 and 200 nm) on blank z-cut quartz substrates and TEM grids concurrently in which nominally targeted Cs:Pb precursor flux ratios spanned a broad parameter range from 0.85:1 (Cs-deficient) to 3:1 (Cs-rich). The thinner 35 nm film type has been optimised for atomic-resolution STEM studies,[39] while 200 nm is representative of a typical gain medium thickness in a film-based perovskite laser. By examining two thicknesses together, we simultaneously elucidate impacts on optical, structural, and atomistic properties when precursor flux ratios are varied. We have here chosen to report changes in stoichiometry via precursor flux ratios from considering the real deposition rate of each individually tooled precursor on z-cut quartz substrates for ease of reproducibility, with full parameters summarized in Table S1 (Supporting Information).

We first examined the set of 200 nm-thick $CsPbBr_3$ films through X-ray diffraction (XRD), with normalized spectra

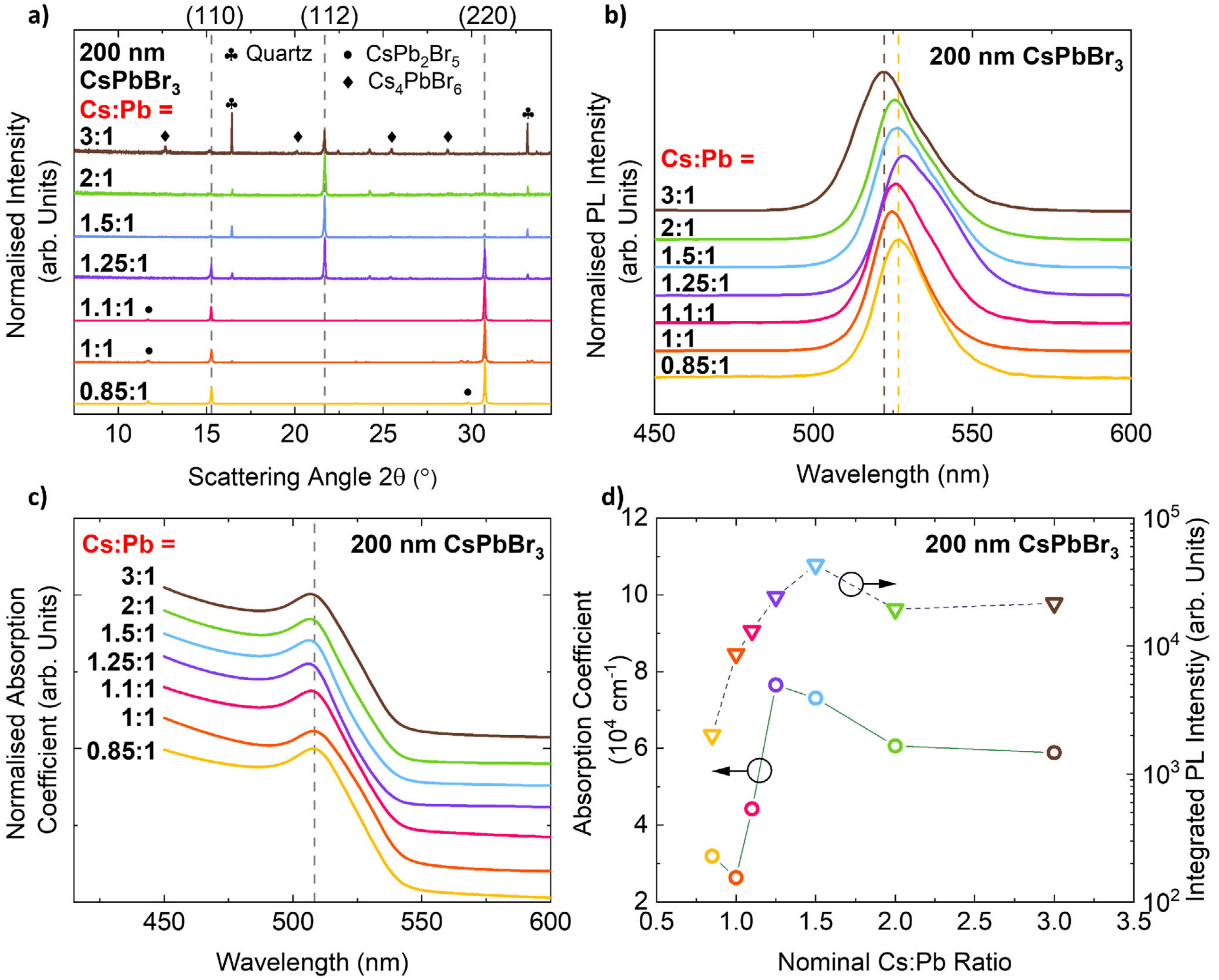

Figure 1. Characterisation of 200 nm-thick CsPbBr$_3$ films with varied Cs:Pb precursor flux ratios. a) X-ray diffraction spectra (XRD) illustrate changes in preferred grain orientations and presences of impurity phases which correspond to a gradual transition from Cs-deficient to Cs-rich preparation conditions. The X-ray source was Cu-K$_\alpha$ $\lambda = 1.54$ Å and each spectrum was corrected for sample displacement. b) Normalized photoluminescence (PL) spectra from photo-excitation of a 398 nm-wavelength continuous-wave laser at a power of 1.1 W cm^{-2}, well below amplified spontaneous emission thresholds of all films. c) Normalized absorption spectra elucidate minimal variations in the optical bandgap despite changes in the nominal Cs:Pb flux ratio. PL and absorption data for different Cs:Pb flux ratios are offset vertically for clarity. Unprocessed PL and absorption data are shown in Figure S6 (Supporting Information). d) Extracted absorption coefficient values at the excitonic peak and integrated PL intensity both plotted against the respective Cs:Pb flux ratio. Solid and dashed lines are indicative guides for eyes only.

presented in **Figure 1a** (unnormalized data are provided in Figure S3, Supporting Information). It is evident that all films exhibit clear features of the orthorhombic γ-CsPbBr$_3$ phase, and we assigned perovskite diffraction peaks at 2θ of 15.1 °, 21.6 °, 25.3 °, and 30.8 ° to 110, 112, 210, and 220 reflections, respectively.[40–42] Meanwhile, XRD peaks corresponding to impurity phases of CsPb$_2$Br$_5$ (2θ of 11.7 ° and 29.4 °) and Cs$_4$PbBr$_6$ (2θ of 12.6 °, 20.1 °, 25.5 °, and 28.6 °) are consistent with Cs:Pb flux ratios employed in co-evaporations.[29,43] Specifically, diffraction peaks of CsPb$_2$Br$_5$ are observed at Cs-deficient (Cs:Pb = 0.85:1), nominally stoichiometric (Cs:Pb = 1:1), and low Cs-excess preparation conditions up to Cs:Pb = 1.1:1. Meanwhile, Cs$_4$PbBr$_6$ characteristic XRD peaks are detected at higher Cs-excess parameters at and above Cs:Pb = 1.5:1. It is important to note that the average Cs:Pb stoichiometry of the film is not expected to exactly match the precursor flux ratio as the relative sticking coefficient of a precursor may change in the presence of another precursor or with the target film material.[44,45]

We observe that the Cs:Pb precursor flux ratio not just controls impurity phases but strongly influences the preferred crystal orientation of the predominant γ-CsPbBr$_3$ phase. At low Cs:Pb flux ratios, γ-CsPbBr$_3$ growth in the [110] direction dominates, however as the Cs:Pb ratio increases the growth planes become more randomized, as indicated by the appearance of 112 peak in XRD results from the Cs:Pb = 1.25:1 to 3:1 films (Figure 1a). This appears to be a general phenomenon as a review of published XRD spectra from vapor-deposited $CsPbBr_3$ with similar thicknesses[29,33] reveals similar changes in orientation with growth conditions (although this trend was not specifically mentioned in these works).

When comparing XRD spectra of thinner 35 nm-thick films (normalized in Figure S4a and unnormalized in Figure S5, Supporting Information), orientational preference of perovskite crystals are considerably different compared to thicker 200-nm films. In thinner films, grains of γ-$CsPbBr_3$ are always preferentially aligned along the [110] direction, despite drastic variations in their Cs:Pb flux ratios. Nevertheless, diffraction peaks corresponding to $CsPb_2Br_5$ are only observed until a Cs:Pb flux ratio of 1:1, which evince that the transition in the final stoichiometry of formed γ-$CsPbBr_3$ from Cs-deficient to Cs-rich still holds. Differences uncovered in XRD spectra across two thicknesses suggest that in the vapor deposition of all-inorganic perovskites, vertical growth of films may not be uniform and there are potentially recrystallization processes as the film thickens. Therefore, a templating approach with a seeding layer, analogously employed in the co-deposition of organic-inorganic perovskites,[45,46] could be considered in further precisely tuning the preferential growth direction of γ-$CsPbBr_3$.

Meanwhile, only minimal shift in emission centres of PL spectra of 200 nm-thick films are observed across the full range of Cs:Pb precursor flux ratios, as indicated by the less than 5 nm spectral shifts in Figure 1b). This is consistent with measurements of absorption coefficient in Figure 1c and associated Elliot fits (Figure S8, Supporting Information), in which changes in the electronic bandgap is less than 0.013 eV across all compositions. These findings suggest that although there are impurities of $CsPb_2Br_5$ or Cs_4PbBr_6, there is no evidence of any strong confinement effect, which would cause both the optical and electronic bandgap to change more considerably.[29] Moreover, these observations also indicate that even under the most Cs-rich co-evaporation condition, the volume fraction of the Cs_4PbBr_6 impurity phase is relatively small compared to the dominant γ-$CsPbBr_3$ phase. All co-deposited films exhibit a strong excitonic peak at around 2.45 eV and a clear absorption onset, with an electronic bandgap of 2.48 eV and an excitonic binding energy E_b of ≈50 meV, extracted from Elliot fittings. Similar measurements on the set of thinner 35-nm films demonstrate an identical trend, in which their PL emission centers and absorption onsets are mostly independent of Cs:Pb flux ratios (Figure S4b, Supporting Information).

Nevertheless, there are significant changes in the intensity of PL emission and absorption coefficient values of both the 35 nm and 200 nm films across varying Cs:Pb flux ratios (Figure 1d and Figure S4d, Supporting Information). In particular, PL emission is strongly quenched under Cs-deficient conditions, whilst the integrated emission intensity increases by an order of magnitude for Cs:Pb = 1.5:1 films of both thicknesses. Further increments of Cs-excess do not lead to any additional enhancement of PL emission in films of both thicknesses. Similarly, values of absorption coefficients at the excitonic peak show the same behavior, in which $CsPbBr_3$ is most strongly absorbing when there is a small Cs-excess, with a maximum value obtained between the Cs:Pb flux ratio of 1.25:1 and 1.5:1. We also considered the number of photons absorbed at the excitonic peak based on the Beer's law for each composition (Figure S10a, Supporting Information) and corrected the integrated PL intensity of all 200 nm-thick films (Figure S10b, Supporting Information) to be independent of number of photons absorbed. We obtained the similar trend to the integrated PL intensity presented in Figure 1d.

Overall, the optimal photo-physical properties of γ-$CsPbBr_3$, i.e. maximum PL emission intensity and absorption coefficient, are found for films grown with a Cs:Pb precursor flux ratio of 1.5:1. These conditions also corresponds to the minimal presence of $CsPb_2Br_5$ and Cs_4PbBr_6 impurities. Therefore, we hypothesize that there is a strong correlation between enhanced photo-physical properties and the relative suppression of impurity phases. As will be discussed in the next section, in conditions of excess Cs where RP defects are observed, it is also important to minimize the density of RP defect to achieve optimal photo-physical properties.

2.2. Microstructural and Atomic-Scale Analysis

From photo-physical and structural measurements, it is clear that a full understanding of thin-film growth, crystallization, and morphology on both microstructural and atomic scales are essential to explain these observed differences across varying Cs:Pb flux ratios. Therefore, we performed low-dose STEM imaging on vapor co-deposited $CsPbBr_3$ films of both thicknesses. **Figure 2** illustrates an overview of the microstructure of thin films with three distinct Cs:Pb flux ratios at low and high imaging magnification. We further identified the perovskite phase in TEM using atomic-resolution Annular Dark Field (STEM-ADF) and four-dimensional scanning transmission electron microscopy (4D-STEM) for thinner 35-nm film specimens (Figure S11, Supporting Information), and 4D-STEM for thicker 200-nm specimens (Figure S12, Supporting Information). In conjunction, we have conducted atomic-resolution STEM-ADF imaging to confirm the presence of impurity phases ($CsPb_2Br_5$ and Cs_4PbBr_6) and to gain atomic-level insights into their structures, which have not been thoroughly investigated previously, as presented in **Figure 3**.

Phase analyses of perovskite grains indicate that co-deposited $CsPbBr_3$, across all Cs:Pb precursor flux ratios and thicknesses, exhibit the orthorhombic γ-phase, consistent with observations from XRD. Meanwhile from thinner 35-nm films, grains corresponding to $CsPb_2Br_5$ impurities can be found in specimens with a Cs:Pb flux ratio up to 1.25:1 (Figure S11a, Supporting Information), while impurities of Cs_4PbBr_6 are present in samples with a Cs:Pb flux ratio of 2:1 or higher (Figure S11b, Supporting Information). In the 200 nm-thick film with Cs:Pb = 1.5:1, a number of grains with higher imaging intensity are seen from the STEM-ADF image in Figure 2g. Results from 4D-STEM elucidate that a small proportion of these "brighter grains" exhibit characteristic electron reflections that can be specifically indexed to the Cs_4PbBr_6 phase (Figure S12, Supporting Information), which indicate the presence of such an impurity and is in good agreement with XRD spectra in Figure S3 (Supporting Information).

We first highlight atomic structures of γ-$CsPbBr_3$ and its associated impurity phases. Figure 3d presents a representative impurity grain observed in 35 nm $CsPbBr_3$ films with a Cs:Pb flux ratio of 0.85:1. The atomic arrangement is consistent with the $CsPb_2Br_5$ phase viewed along the [110] zone axis. In this structure, Cs/Br mixed columns are surrounded by eight columns

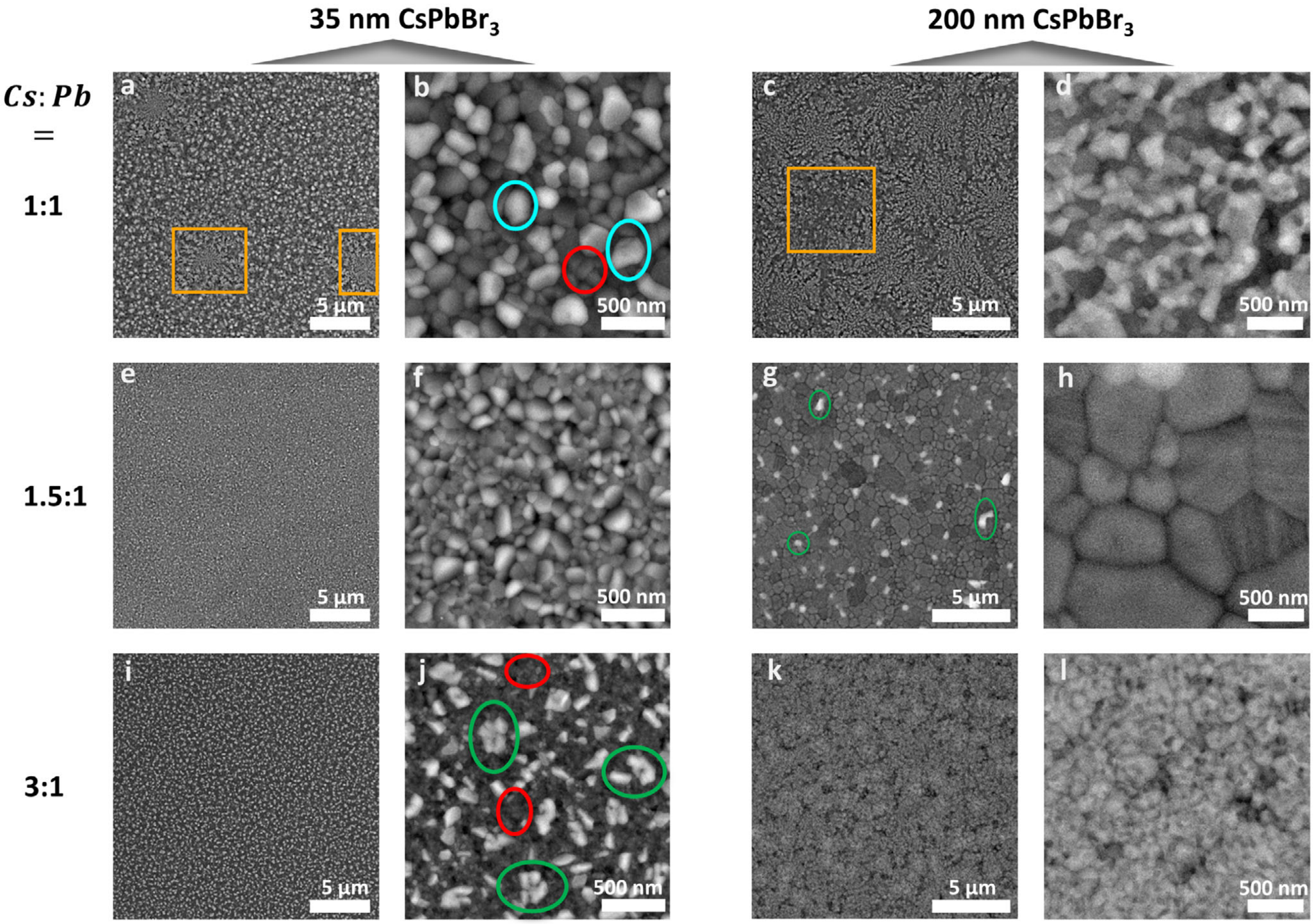

Figure 2. Annular Dark Field (STEM-ADF) images of vapour-deposited $CsPbBr_3$. Studied specimens are co-evaporated with conditions of a,b) 35 nm-thick with a Cs:Pb precursor flux ratio of 1:1; c,d) 200 nm-thick with a Cs:Pb flux ratio of 1:1; e,f) 35 nm-thick with a Cs:Pb flux ratio of 1.5:1; g,h) 200 nm-thick with a Cs:Pb flux ratio of 1.5:1; i,j) 35 nm-thick with a Cs:Pb flux ratio of 3:1; k,l) 200 nm-thick with a Cs:Pb flux ratio of 3:1. Red circles indicate representative grains corresponding to the γ-$CsPbBr_3$ phase; blue circles or green circles indicate representative grains with an impurity phase of $CsPb_2Br_5$ or Cs_4PbBr_6, respectively. Orange boxes highlight "snowflake"-like microstructural features in films with a Cs:Pb flux ratio of 1:1.

containing alternating Cs and Pb atoms, accommodating the excess $PbBr_2$ composition in the unit cell relative to the stoichiometric $CsPbBr_3$ perovskite phase.

In contrast, all grains in 35 nm-thick Cs:Pb = 1.5:1 films are identified as the γ-$CsPbBr_3$ phase, predominantly aligned along the [110] zone axis, as shown in the example in Figure 3e. Further increases in the Cs content (Cs:Pb $\geqslant$ 1.5:1) lead to the formation of the Cs_4PbBr_6 impurity phase, which is illustrated in Figure 3f. When viewed along the [201] zone axis, the high-intensity Pb atomic layers are sandwiched between lower-intensity Cs layers, consistent with the crystal model in Figure 3c. Based on the unit cell structure, two additional Cs layers surround each Pb layer, although they are not clearly resolved in the image due to their close lattice spacing. These observations suggest that Cs-excess at higher Cs:Pb flux ratio is accommodated by the formation of the Cs_4PbBr_6 phase, which possesses a Cs-rich unit cell structure.

In the meantime, we uncover stunning differences in microstructures of γ-$CsPbBr_3$ films when Cs:Pb flux ratios are varied. Considering images from 35 nm-thick specimens, it is evident that morphological homogeneity is promoted from introducing Cs-excess during co-depositions. In Cs-deficient (Cs:Pb = 0.85:1) and nominally stoichiometric (Cs:Pb = 1:1) conditions, "snowflake" features (highlighted with orange boxes) have formed in these films (Figure 2a; Figure S13a,b, Supporting Information). Indeed, upon closer examination with a higher magnification, a different image intensity for grains corresponding to $CsPb_2Br_5$ and γ-$CsPbBr_3$ is identified (Figure 2b; Figure S14a,b, Supporting Information). These features indicate rather poor and possibly incomplete crystallization dynamics of the resulting film, in which mixed-phase grains are formed in random shapes. In contrast, with further increments of the Cs:Pb flux ratio, more consistent and uniform microstructures are uncovered, particularly for the Cs:Pb = 1.5:1 flux films in Figure 2e,f. Not only the specimen is free of all secondary impurity phases, but also perovskites with well-defined shapes are seen. Some of these grains are in excess of 100 nm wide, indicating an excellent crystallization process, especially when the film is only 35 nm thick. Further addition of Cs-excess (Cs:Pb $\geqslant$ 2:1) results in the considerable presence of Cs_4PbBr_6 impurity phase intermixed with γ-$CsPbBr_3$ grains, which is suggested by the significant difference in image intensity associated with different grains in Figure 2i,j and Figures S13e,f and S14e,f (Supporting Information).

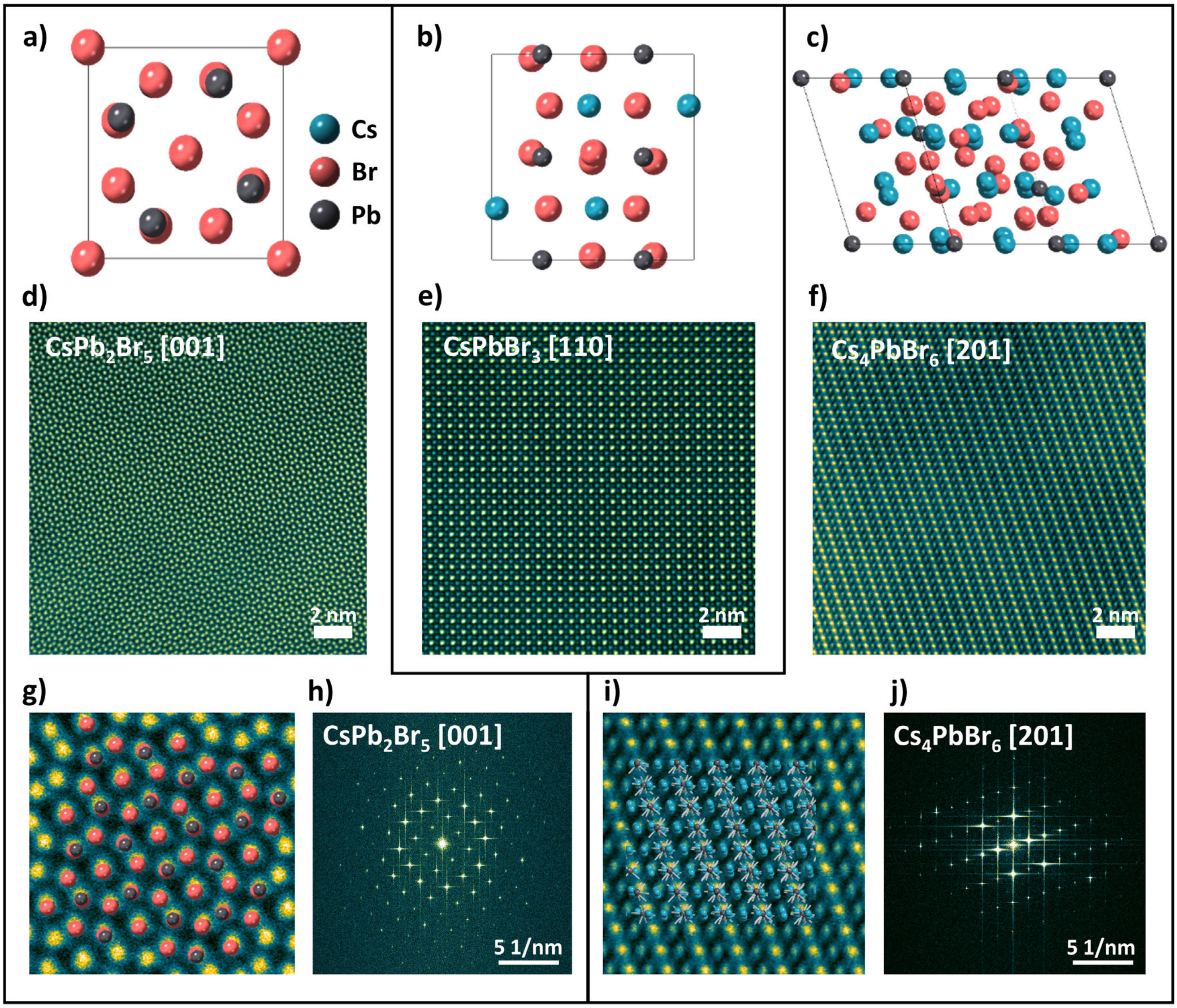

Figure 3. Atomic-resolution studies of CsPbBr$_3$ and its impurity phases. Schematic diagram illustrating the unit cell structure of a) CsPb$_2$Br$_5$ in the [001] direction, b) γ-CsPbBr$_3$ in the [110] direction, and c) Cs$_4$PbBr$_6$ in the [201] direction. STEM-ADF image of d) CsPb$_2$Br$_5$, e) γ-CsPbBr$_3$, and f) Cs$_4$PbBr$_6$. g) Zoomed in STEM-ADF image of CsPb$_2$Br$_5$ and overlaid with its crystal model. h) Fourier Transform (FT) image of CsPb$_2$Br$_5$. i) Zoomed in STEM-ADF image of Cs$_4$PbBr$_6$ and overlaid with its crystal model. j) FT image of Cs$_4$PbBr$_6$.

For thicker 200-nm films, almost identical differences in microstructures are observed. Under preparation conditions of both Cs:Pb = 1:1 and 3:1, in which either the CsPb$_2$Br$_5$ or Cs$_4$PbBr$_6$ impurity phase is present, undesirable morphological features are obtained. For example, "snowflake"-like microstructures in Figure 2c,d entail that grains are stacked and piled together randomly in both vertical and horizontal directions. Similarly, with a large Cs-excess flux ratio, in Figure 2k,l, films have failed to crystallize into distinctive large-size and well-defined shape grains. In contrast, for films with Cs:Pb = 1.5:1 flux ratio in Figure 2g,h, changing deposition thickness from 35 to 200 nm results in the further enlargement of grains with a well-defined shape, with some grains being almost 500 nm in size. These findings indicate an excellent crystallization process in Cs:Pb = 1.5:1 films with both thicknesses. As a result, a homogenous, uniform, and compact film morphology with highly oriented growth was achieved. These features are highly beneficial in relation to both observed enhancement in PL emission and absorption coefficient in films of the same flux ratio (Cs:Pb = 1.5:1) in Figure 1 and Figure S4 (Supporting Information), respectively owing to the consequential reduction of both radiative recombination centers and light scattering from improved crystallization.

We further scrutinized STEM images corresponding to a single grain in search of RP defects (Figure S15, Supporting Information), which act as non-radiative trapping-sites for photo-excited charge carriers.[39] In a RP defect, there is a displacement of lattice planes by half a unit cell in the in-plane direction parallel to the defect, leading to an insertion of an additional Cs-plane, or equivalently, the removal of a Pb-plane.[39,47,48] Therefore, an excess of CsX is the most important prerequisite in forming RP defects as these defects lead to a locally Cs-rich composition.[39,49] We do not observe any RP defects for Cs-deficient or nominally stoichiometric conditions, and RP defects only begin to emerge on grain boundaries for flux ratios of Cs:Pb $\geqslant$ 1.5:1. The planar defects observed under Cs-excess conditions are identified as RP defects, corresponding to a local Cs_2PbBr_4 structure, i.e., the $n = 1$ member of the general RP formula $A_{n+1}B_nX_{3n+1}$. Linear density of RP defects from the representative grain increases significantly for Cs:Pb = 2:1 and 3:1 specimens, in which defects can be observed both near all grain boundaries and in the center of the grain. Here, we deduced the RP defect density via accounting the sum of the atomic length of each RP fault, and factored over the size of the STEM imaging spot.[39] Additional images of different grains of the 35 nm-thick specimens with Cs:Pb flux ratio of 3:1 are presented in Figure S16 (Supporting Information), which all illustrate consistent presence of a significant number of planar faults. The trend observed for RP-defect density is consistent with previous phase analysis: for precursor flux conditions of both Cs-deficient and Cs:Pb < 1.5:1, the $CsPb_2Br_5$ impurity phase forms and there is no RP fault; and whilst for Cs:Pb $\geqslant$ 1.5:1, Cs-rich parameters promote formations of the Cs_4PbBr_6 impurity phase and therefore leading to an increase in the RP-defect density. More importantly, as uncovered in the analogous γ-$CsPbI_3$ system, RP defect density directly correlate with both quenched PL emission and shortened charge-carrier lifetimes, owing to enhanced rate of trap-assisted recombination.[39] Thus, increasing density of RP faults formed in γ-$CsPbBr_3$ specimens with higher Cs-excess contributes to the reduction in both thin-film absorption and PL intensity (Figure 1 and Figure S4, Supporting Information) when the Cs:Pb flux ratio is incremented beyond 1.5:1.

2.3. Correlation to Amplified Spontaneous Emission Characteristics

From both photo-physical and STEM investigations, we identified that vapor-deposited films with a Cs:Pb precursor flux ratio of 1.5:1 for both thicknesses of 35 and 200 nm were the most promising optical gain media. Hence, we probed ASE characteristics of the same sets of thin film excited by 35 fs duration and 3.1 eV (400 nm in wavelength) photon energy laser pulses. As the ASE threshold has been shown to be dependent on an array of factors including pump beam spot size and geometry of pump and collection optics,[9,29] we kept measurement conditions the same for all films to probe any relative changes when the Cs:Pb flux ratio or the film thickness is varied. In our system, the pump beam photo-excites the sample at normal incidence, with emitted PL collected at an approximate angle of 45° relative to the incident laser beam (full details in Supporting Information). Extracted ASE thresholds for both 200 nm- and 35 nm-thick sets of $CsPbBr_3$ films are displayed in **Figure** 4a,b.

For thicker 200-nm films, higher ASE thresholds are observed in $CsPbBr_3$ films with Cs-deficient and nominally stoichiometric preparation conditions. The ASE threshold further reduces as the Cs:Pb flux ratio is increased, in which a lowest threshold fluence of 30.9 $\mu J\ cm^{-2}$ is deduced at a Cs:Pb flux ratio of 1.5:1, as expected from previous optical and structural characterisation results. At higher Cs-rich flux ratios of 2:1 and 3:1, ASE thresholds increase slightly, which is consistent with a reduction of their respective integrated PL intensity in Figure 1d and formation of RP defects (Figure S15, Supporting Information). These findings suggest that at higher Cs-excess conditions, correlation of optically driven emissions may be much more nuanced than just the presence of Cs_4PbBr_6 impurities previously reported.[29,33] The set of thinner 35-nm films exhibit very similar ASE behaviours to thicker 200-nm films. A decreasing trend in thresholds is observed between the Cs:Pb = 1:1 and Cs:Pb = 1.5:1 films, and the ASE threshold further increases when additional CsBr is incorporated. No characteristic ASE peak was identified for 35 nm-thick films with a Cs:Pb flux ratio of either 0.85:1 or 3:1, even when the exciting laser fluence was increased to either 425.2 $\mu J\ cm^{-2}$ or 543.6 $\mu J\ cm^{-2}$ respectively. The lowest ASE threshold recorded for thinner films is 34.9 $\mu J\ cm^{-2}$, also at a Cs:Pb flux ratio of 1.5:1.

Figure 4c presents power-dependent PL spectra of the 200 nm-thick film with an optimal flux ratio Cs:Pb = 1.5:1 near its ASE threshold. The broad SE peak, which has a full width half maximum (FWHM) of ≈40 nm is quickly overtaken by the presence of a narrower and strongly emissive ASE peak with a FWHM of 10 nm. The inset also illustrates the extraction of ASE threshold through fitting the fluence-dependent SE peak or ASE peak intensities. Corresponding spectra, emission intensity, and FWHM analysis of the thinner 35-nm film with a Cs:Pb flux ratio of 1.5:1 are shown in Figure S18. Full power-dependent PL spectra and fitting of ASE thresholds for all studied $CsPbBr_3$ thin films are included in Figures S19–S22 (Supporting Information).

Finally, we hypothesize possible correlations between atomistic findings and ASE thresholds of vapor-deposited $CsPbBr_3$ when Cs:Pb flux ratios are varied. Under both Cs-deficient and large Cs-excess precursor flux conditions, formation of $CsPb_2Br_5$ and Cs_4PbBr_6 impurity phases are associated with poor crystallization of specimens during vapor co-depositions of γ-$CsPbBr_3$. This inhibits the uniform and homogenous growth of perovskite grains, in which the poor surface morphology contributes to a suppressed radiative recombination and undesirable ASE threshold. Considerable linear density of planar RP defects also forms under high Cs-excess preparation parameters, acting as a major source of non-radiative recombination centers, further reducing the luminescence efficiency and increasing ASE thresholds. Nevertheless, we identified that at a Cs:Pb flux ratio of 1.5:1, films possess a complete crystallization process, as exhibited from large and consistent grains with clearly defined shapes and dimensions. It is possible that a small amount of excess-Cs during growth assists with more complete nucleation owing to higher kinetic energy from the CsBr vapor.[32] Therefore, these excellent microstructures in films grown under a flux ratio of Cs:Pb = 1.5:1 attribute to lower light-scattering in the 200 nm-thick films, and hence reduced photon-out-coupling, which is supported by a low ASE threshold.

Looking ahead, observation of a small density of secondary Cs_4PbBr_6 phases in these films (Figure 2g) and RP defects (Figure S15, Supporting Information) even in the best (Cs:Pb flux = 1.5:1) films suggest further fine-optimisation in Cs:Pb precursor flux ratios during vapor co-deposition and post-deposition processing. Such optimization is likely to further reduce of the ASE threshold and improve the photo-physical properties of γ-$CsPbBr_3$ through removal of Cs_4PbBr_6 phases and RP defects.

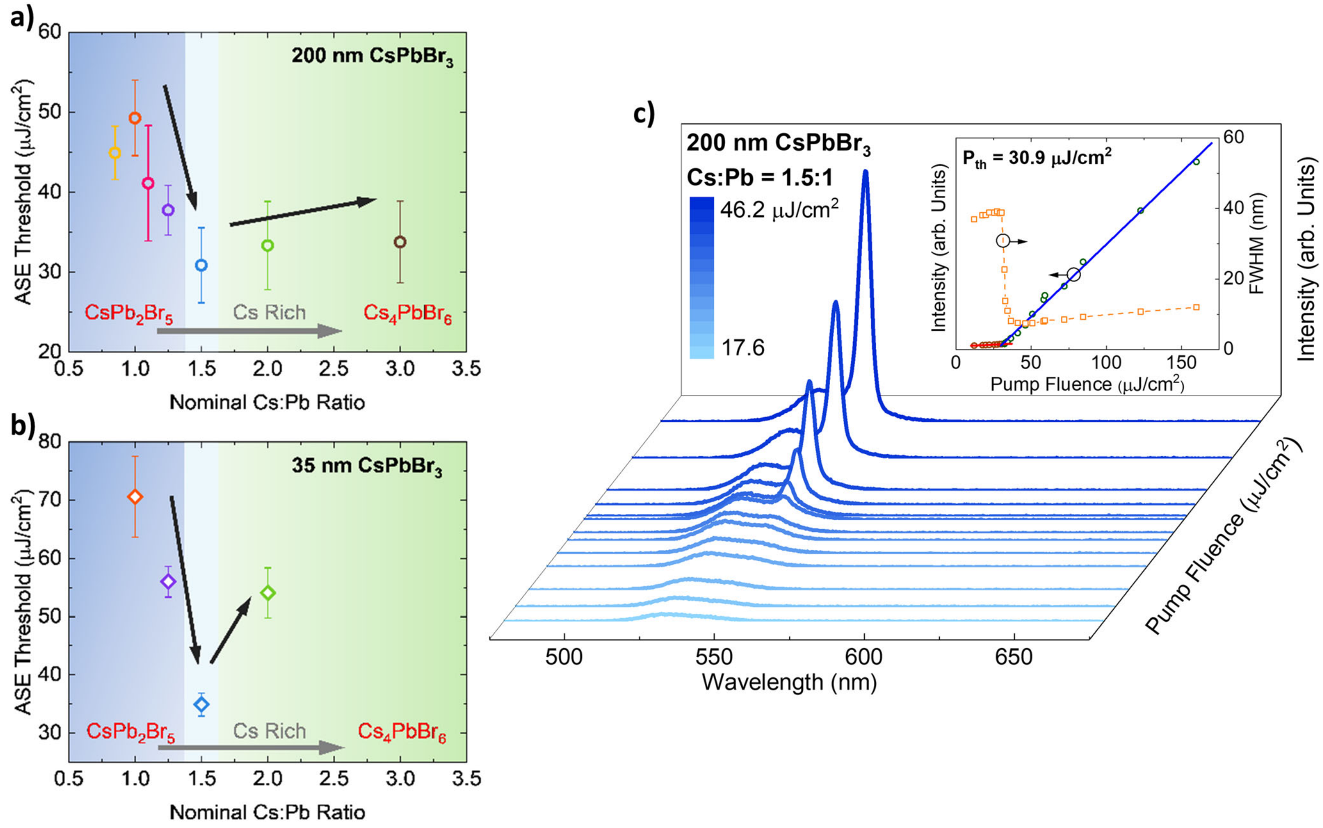

Figure 4. Amplified spontaneous emission (ASE) characteristics of $CsPbBr_3$ films. a) ASE thresholds of 200 nm-thick $CsPbBr_3$ films with different Cs:Pb precursor flux ratios in co-evaporation. b) ASE thresholds of 35 nm-thick $CsPbBr_3$ films. c) Power-dependent PL spectra of 200 nm optimal Cs:Pb = 1.5:1 thin film with excitation density near the ASE threshold. The inset illustrates the spontaneous emission peak intensity and the full width half maximum (FWHM) plotted against the pump fluence. Photo-excitation was from a pulsed Ti:Sapphire laser frequency-doubled with BBO to 400 nm-wavelength, and error bars in ASE thresholds indicate uncertainties from linear fits of spontaneous emission peak intensities.

3. Conclusion

To summarize, we performed a novel study on vapour co-deposited γ-$CsPbBr_3$ thin films with varying Cs:Pb stoichiometries, and investigated their photo-physical, structural, and atomic-scale properties. We highlighted that across two film thicknesses, films with a molar Cs:Pb precursor flux ratio of 1.5:1 exhibit most optimal microstructures, including homogenous and uniform morphology as well as the relative suppression of planar RP defects. As a result of these improvements, enhanced PL emission and optimized ASE threshold were measured. From STEM, we further revealed the formation dynamics and precise atomic structures of impurity phases of $CsPb_2Br_5$ and Cs_4PbBr_6 through unambiguous atomic-resolution imaging. This study demonstrates a facile method of optimizing γ-$CsPbBr_3$ from vapor-processing, yielding films suitable for low threshold lasers.

4. Experimental Section

Sample Preparation

Z-cut quartz substrates (UQG Ltd.) were sonicated for 5 min each in fresh Decon-90 solution (1% volume in de-ionized water), de-ionized water, acetone, and isopropyl alcohol sequentially. Prior to thin-film deposition, quartz substrates and TEM grids (Agar scientific, Cu-400 mesh) were O_2-plasma treated for 10 min and 0.3 min, respectively.

$CsPbBr_3$ thin films were co-deposited in our custom-built thermal evaporator. The chamber was pumped down to a base pressure less than 3×10^{-6} mbar before the commencement of all depositions. The surrounding walls of the evaporation chamber were maintained at 17 °C, while the rotating substrate was kept at 20 °C through two separate chillers. A customized interface was employed for deposition control and deposition rates were monitored through gold-plated quartz crystal microbalances. $PbBr_2$ (Alfa-Aeser, 99.998%, metals base) and CsBr (Alfa-Aeser, 99.9% metals base) were chosen as precursors. Starting from the stoichiometric composition, where Cs:Pb precursor flux ratio was aimed at nominally 1:1, further changes to the nominal Cs:Pb ratios were achieved by holding the $PbBr_2$ evaporation rate constant and only varying the CsBr evaporation rate. All deposition rates were halved for the thinner films. As-deposited films were annealed at 200 °C in N_2 atmosphere for 2 min (thinner, nominally 35-nm films) or 10 min (thicker, nominally 200-nm films). Detailed methods and evaporation parameters are elaborated in the Supporting Information.

Thin-Film Characterization and Microscopy

Transmission-Reflection measurements were performed on a Bruker Vertex 80v Fourier Transform interferometer, with a tungsten-halogen near-infrared source, CaF_2 beam splitter, and a silicon diode detector.

XRD patterns were measured with a Panalytical X'pert powder diffractometer with copper X-ray source (Cu-K_{α}, $\lambda = 1.54$ Å set at 40 kV and 40 mA).

Steady-state PL measurements were performed through photoexcitation of $CsPbBr_3$ thin films with a 398 nm-wavelength continuous wave laser (PicoHarp, LDH-D-C-405M) with a power density of 1.1 W cm^{-2} from the perovskite side.

Power-dependent steady-state PL were further measured to probe ASE characteristics of $CsPbBr_3$ on a separate pulsed laser system. Thin films under investigation were photo-excited at 400 nm-wavelength by an amplified and frequency-doubled Spectra-Physics Spitfire Ti:Sapphire laser with a repetition rate of 2.5 kHz. The pump laser is directed at normal incidence to all thin films, with PL collected an angle of 45° relative to the incident laser beam. Average incident power was varied from 0.26 mW to 10.29 mW, through changing a ND filter wheel.

STEM-ADF and 4D-STEM data were taken using a Thermo Fisher Scientific Spectra ϕ FEG-TEM and a FEI Titan^3 80-300 FEG-TEM, both equipped with probe and imaging spherical aberration correctors. Images were acquired at 300 kV, using a 15 mrad probe-forming aperture, and a detector collection angle between 39 and 200 mrad. 4D-STEM datasets were collected using an electron microscope pixel array detector, with 256×256 probe positions, 128×128 pixel diffraction patterns acquired at 1 kHz.

Author Contributions

M.B.J. designed the study and supervised the project. Q.Y. fabricated thin-film samples, performed XRD, photo-physical, and ASE measurements, and analyzed data. W.L. and J.E. designed and carried out TEM experiments and analyzed data. F.M.W. assisted with ASE measurements. V.J.Y.L. and L.M.H. performed Elliot fittings on absorption data. Q.Y. and M.B.J. prepared the manuscript. All authors contributed to the discussion of the results and revision of the manuscript.

Supporting Information

Supporting Information is available from the Wiley Online Library or from the author.

Acknowledgements

This research was funded by the EPSRC UK via grants EP/X038777/1 and EP/T025077/1, the Leverhulme Trust via grant RPG-2022-272, Australian Research Council (ARC) Discovery Project DP200103070, and ARC Laureate Fellowship FL220100202. V.J.Y.L. acknowledges financial funding from EPSRC Doctoral Prize.

Conflict of Interest

The authors declare no conflict of interest.

Data Availability Statement

The data that support the findings of this study are available from the corresponding author upon reasonable request.

Keywords

amplified spontaneous emission, atomic-scale microstructures, impurities and defects, metal halide perovskite, vapor deposition

Received: July 7, 2025
Revised: August 18, 2025
Published online:

[1] A. Kojima, K. Teshima, Y. Shirai, T. Miyasaka, *J. Am. Chem. Soc.* **2009**, *131*, 6050.
[2] Y.-H. Lin, Vikram, F. Yang, X.-L. Cao, A. Dasgupta, R. D. Oliver, A. M. Ulatowski, M. M. McCarthy, X. Shen, Q. Yuan, M. G. Christoforo, F. S. Y. Yeung, M. B. Johnston, N. K. Noel, L. M. Herz, M. S. Islam, H. J. Snaith, *Science* **2024**, *384*, 767.
[3] J. Luo, J. Li, L. Grater, R. Guo, A. R. b. Mohd Yusoff, E. Sargent, J. Tang, *Nat. Rev. Mater.* **2024**, *9*, 282.
[4] Y. Shi, X. Deng, Y. Gan, L. Xu, Q. Zhang, Q. Xiong, *Adv. Mater.* **2025**, 2413559.
[5] P. Du, J. Li, L. Wang, L. Sun, X. Wang, X. Xu, L. Yang, J. Pang, W. Liang, J. Luo, Y. Ma, J. Tang, *Nat. Commun.* **2021**, *12*, 4751.
[6] Y. Hassan, J. H. Park, M. L. Crawford, A. Sadhanala, J. Lee, J. C. Sadighian, E. Mosconi, R. Shivanna, E. Radicchi, M. Jeong, C. Yang, H. Choi, S. H. Park, M. H. Song, F. De Angelis, C. Y. Wong, R. H. Friend, B. R. Lee, H. J. Snaith, *Nature* **2021**, *591*, 72.
[7] Z. Liu, W. Qiu, X. Peng, G. Sun, X. Liu, D. Liu, Z. Li, F. He, C. Shen, Q. Gu, F. Ma, H.-L. Yip, L. Hou, Z. Qi, S.-J. Su, *Adv. Mater.* **2021**, *33*, 2103268.
[8] L. Lei, Q. Dong, K. Gundogdu, F. So, *Adv. Funct. Mater.* **2021**, *31*, 2010144.
[9] A. L. Alvarado-Leaños, D. Cortecchia, G. Folpini, A. R. Srimath Kandada, A. Petrozza, *Adv. Opt. Mater.* **2021**, *9*, 2001773.
[10] S. Huang, Z. Shen, Y. Liao, Z. Liu, Z. Hu, Q. Li, Z. Zhang, S. Dong, J. Luo, J. Du, J. Tang, Y. Leng, *Adv. Mater.* **2023**, *35*, 2306102.
[11] C.-S. J. Wu, A. Olivati, G. Folpini, H. Wang, A. Petrozza, *Adv. Mater.* **2024**, 2407652.
[12] N. Pourdavoud, T. Haeger, A. Mayer, P. J. Cegielski, A. L. Giesecke, R. Heiderhoff, S. Olthof, S. Zaefferer, I. Shutsko, A. Henkel, D. Becker-Koch, M. Stein, M. Cehovski, O. Charfi, H.-H. Johannes, D. Rogalla, M. C. Lemme, M. Koch, Y. Vaynzof, K. Meerholz, W. Kowalsky, H.-C. Scheer, P. Görrn, T. Riedl, *Adv. Mater.* **2019**, *31*, 1903717.
[13] Q. Dong, X. Fu, D. Seyitliyev, K. Darabi, J. Mendes, L. Lei, Y.-A. Chen, C.-H. Chang, A. Amassian, K. Gundogdu, F. So, *ACS Photonics* **2022**, *9*, 3124.
[14] L. Zhang, F. Yuan, H. Dong, B. Jiao, W. Zhang, X. Hou, S. Wang, Q. Gong, Z. Wu, *ACS Appl. Mater. Interfaces* **2018**, *10*, 40661.
[15] C. Wang, G. Dai, J. Wang, M. Cui, Y. Yang, S. Yang, C. Qin, S. Chang, K. Wu, Y. Liu, H. Zhong, *Nano Lett.* **2022**, *22*, 1338.
[16] T. J. Evans, A. Schlaus, Y. Fu, X. Zhong, T. L. Atallah, M. S. Spencer, L. E. Brus, S. Jin, X.-Y. Zhu, *Adv. Opt. Mater.* **2018**, *6*, 1700982.
[17] Q. Shang, M. Li, L. Zhao, D. Chen, S. Zhang, S. Chen, P. Gao, C. Shen, J. Xing, G. Xing, B. Shen, X. Liu, Q. Zhang, *Nano Lett.* **2020**, *20*, 6636.
[18] E. J. Juarez-Perez, Z. Hawash, S. R. Raga, L. K. Ono, Y. Qi, *Energy Environ. Sci.* **2016**, *9*, 3406.
[19] T. Burwig, W. Franzel, P. Pistor, *J. Phys. Chem. Lett.* **2018**, *9*, 4808.
[20] J. Moon, Y. Mehta, K. Gundogdu, F. So, Q. Gu, *Adv. Mater.* **2024**, *36*, 2211284.
[21] M. Liu, M. B. Johnston, H. J. Snaith, *Nature* **2013**, *501*, 395.
[22] J. Feng, Y. Jiao, H. Wang, X. Zhu, Y. Sun, M. Du, Y. Cao, D. Yang, S. F. Liu, *Energy Environ. Sci.* **2021**, *14*, 3035.
[23] H. Li, J. Zhou, L. Tan, M. Li, C. Jiang, S. Wang, X. Zhao, Y. Liu, Y. Zhang, Y. Ye, W. Tress, C. Yi, *Sci. Adv.* **2022**, *8*, eabo7422.
[24] Q. Yuan, K. B. Lohmann, R. D. Oliver, A. J. Ramadan, S. Yan, J. M. Ball, M. G. Christoforo, N. K. Noel, H. J. Snaith, L. M. Herz, M. B. Johnston, *ACS Appl. Mater. Interfaces* **2022**, *15*, 772.
[25] J. Borchert, R. L. Milot, J. B. Patel, C. L. Davies, A. D. Wright, L. Martinez Maestro, H. J. Snaith, L. M. Herz, M. B. Johnston, *ACS Energy Lett.* **2017**, *2*, 2799.
[26] D. Forgács, L. Gil-Escrig, D. Pérez-Del-Rey, C. Momblona, J. Werner, B. Niesen, C. Ballif, M. Sessolo, H. J. Bolink, *Adv. Energy Mater.* **2017**, *7*, 1602121.
[27] Y. Vaynzof, *Adv. Energy Mater.* **2020**, *10*, 2003073.

[28] A. Paliwal, K. P. Zanoni, C. Roldán-Carmona, N. Rodkey, H. J. Bolink, *ACS Energy Lett.* **2024**, *9*, 4587.
[29] H. Tian, X. Jiang, T. Li, M. Yan, L. Xu, G. Lu, Y. Zhang, H. Zhu, H. He, D. Yang, Y. Fang, *Small* **2022**, *18*, 2204752.
[30] K. Jia, L. Song, Y. Hu, X. Guo, X. Liu, C. Geng, S. Xu, R. Fan, L. Huang, N. Luan, W. Bi, *ACS Appl. Mater. Interfaces* **2020**, *12*, 15928.
[31] N. Kim, M. Shin, S. Jun, B. Choi, J. Kim, J. Park, H. Kim, W. Jung, J.-Y. Lee, Y.-H. Cho, B. Shin, *ACS Appl. Mater. Interfaces* **2021**, *13*, 37323.
[32] J. Li, P. Du, Q. Guo, L. Sun, Z. Shen, J. Zhu, C. Dong, L. Wang, X. Zhang, L. Li, C. Yang, J. Pan, Z. Liu, B. Xia, Z. Xiao, J. Du, B. Song, L. Jiajun, J. Tang, *Nat. Photonics* **2023**, *17*, 435.
[33] Y. Mao, C. Liang, G. Wang, Y. Wang, Z. Zhang, B. Wang, Z. Wen, Z. Mu, G. Sun, S. Chen, G. Xing, *Adv. Opt. Mater.* **2022**, *10*, 2201845.
[34] L. N. Quan, R. Quintero-Bermudez, O. Voznyy, G. Walters, A. Jain, J. Z. Fan, X. Zheng, Z. Yang, E. H. Sargent, *Adv. Mater.* **2017**, *29*, 1605945.
[35] S.-H. Chin, D. Cortecchia, M. Forzatti, C.-S. Wu, A. L. Alvarado-Leanos, G. Folpini, A. Treglia, I. A. Kalluvila Justin, A. Paliwal, C. Cho, C. Roldán-Carmona, M. Sessolo, A. Petrozza, H. Bolink, *Adv. Opt. Mater.* **2024**, *12*, 2302701.
[36] N. Pourdavoud, T. Haeger, A. Mayer, P. J. Cegielski, A. L. Giesecke, R. Heiderhoff, S. Olthof, S. Zaefferer, I. Shutsko, A. Henkel, D. Becker-Koch, M. Stein, M. Cehovski, O. Charfi, H.-H. Johannes, D. Rogalla, M. C. Lemme, M. Koch, Y. Vaynzof, K. Meerholz, W. Kowalsky, H.-C. Scheer, P. Görrn, T. Riedl, *Adv. Mater.* **2019**, *31*, 1903717.
[37] M. U. Rothmann, J. S. Kim, J. Borchert, K. B. Lohmann, C. M. O'Leary, A. A. Sheader, L. Clark, H. J. Snaith, M. B. Johnston, P. D. Nellist, L. M. Herz, *Science* **2020**, *370*, eabb5940.
[38] W. Li, M. Hao, A. Baktash, L. Wang, J. Etheridge, *Nat. Commun.* **2023**, *14*, 8523.
[39] W. Li, Q. Yuan, Y. Chen, J. R. Lilly, M. R. Filip, L. M. Herz, M. B. Johnston, J. Etheridge, *Adv. Mater.* **2025**, *37*, 2501788.
[40] Z.-J. Yong, Y. Zhou, J.-P. Ma, Y.-M. Chen, J.-Y. Yang, Y.-L. Song, J. Wang, H.-T. Sun, *ACS Appl. Mater. Interfaces* **2017**, *9*, 32920.
[41] M. Shin, H. S. Lee, Y. C. Sim, Y.-H. Cho, K. Cheol Choi, B. Shin, *ACS Appl. Mater. Interfaces* **2019**, *12*, 1944.
[42] S. Xie, A. Osherov, V. Bulović, *APL Mater.* **2020**, *8*, 051113.
[43] Y. Ling, L. Tan, X. Wang, Y. Zhou, Y. Xin, B. Ma, K. Hanson, H. Gao, *J. Phys. Chem. Lett.* **2017**, *8*, 3266.
[44] J. Borchert, I. Levchuk, L. C. Snoek, M. U. Rothmann, R. Haver, H. J. Snaith, C. J. Brabec, L. M. Herz, M. B. Johnston, *ACS Appl. Mater. Interfaces* **2019**, *11*, 28851.
[45] S. Yan, J. B. Patel, J. E. Lee, K. A. Elmestekawy, S. R. Ratnasingham, Q. Yuan, L. M. Herz, N. K. Noel, M. B. Johnston, *ACS Energy Lett.* **2023**, *8*, 4008.
[46] V. Skorjanc, A. Miaskiewicz, M. Roß, S. Maniyarasu, S. Severin, M. R. Leyden, P. Holzhey, F. Ruske, L. Korte, S. Albrecht, *ACS Energy Lett.* **2024**, *9*, 5639.
[47] S. Ruddlesden, P. Popper, *Acta Crystallogr.* **1958**, *11*, 54.
[48] Y.-H. Song, J. Ge, L.-B. Mao, K.-H. Wang, X.-L. Tai, Q. Zhang, L. Tang, J.-M. Hao, J.-S. Yao, J.-J. Wang, T. Ma, J.-N. Yang, Y.-F. Lan, X.-C. Ru, L.-Z. Feng, G. Zhang, Y. Lin, Q. Zhang, H.-B. Yao, *Sci. Adv.* **2022**, *8*, eabq2321.
[49] L. Wang, L. Li, S. Jia, W. Meng, Y. Cheng, Z. Liu, L. Li, S. Yan, Y. Gao, J. Wang, J. Tang, *Adv. Funct. Mater.* **2023**, *33*, 2210286.